JGR Space Physics

RESEARCH ARTICLE
10.1029/2023JA031511

The Structure of the Warped Io Plasma Torus Constrained by the Io Footprint

Stephan Schlegel[1] **and Joachim Saur**[1]

[1]Institut für Geophysik und Meteorologie, Universität zu Köln, Cologne, Germany

Key Points:

- Based on the Io Footprint positions, we show quantitatively that the Io Plasma Torus is centered on the centrifugal equator of Jupiter's multipole magnetic field
- Position of the Io Footprint can be used to constrain a density model of the Io Plasma Torus
- The displacement of the Io Plasma Torus due to higher magnetic field moments can change the plasma density at Io by up to 20%

Correspondence to:

S. Schlegel,
sschleg1@uni-koeln.de

Citation:

Schlegel, S., & Saur, J. (2023). The structure of the warped Io Plasma Torus constrained by the Io Footprint. *Journal of Geophysical Research: Space Physics*, *128*, e2023JA031511. https://doi.org/10.1029/2023JA031511

Received 21 MAR 2023
Accepted 3 SEP 2023

Author Contributions:

Conceptualization: Stephan Schlegel, Joachim Saur
Data curation: Stephan Schlegel
Formal analysis: Stephan Schlegel
Investigation: Stephan Schlegel, Joachim Saur
Methodology: Stephan Schlegel, Joachim Saur
Software: Stephan Schlegel
Validation: Stephan Schlegel
Visualization: Stephan Schlegel
Writing – original draft: Stephan Schlegel

Abstract Standard models of force balance along Jovian field lines predict the location of the Io Plasma Torus to be the centrifugal equator of Jupiter's magnetosphere, that is, the position along the magnetic field lines farthest away from Jupiter's rotational axis. In many models, the centrifugal equator is assumed to lay on a plane, calculated from a (shifted) dipole magnetic field, rather than on a warped surface which incorporates Jupiter's higher magnetic field moments. In this work, we use Hubble Space Telescope observations of the Io Main Footprint to constrain density, scale height, and lateral position of the Io Plasma Torus. Therefore, we employ the leading angle of the footprints to calculate expected travel times of Alfvén waves and carry out an inversion of the observations. For the magnetic field, we use the JRM33 magnetic field model. The inversion results show peak densities between $\rho_0 = 1{,}830$ cm^{-3} and $\rho_0 = 2{,}032$ cm^{-3} and scale heights between $H = 0.92R_J$ and $H = 0.97R_J$ consistent with current literature values. Using a warped multipole centrifugal equator instead of a planar dipole increases the quality of the fit by about 25%. We additionally develop two tests to confirm that the multipole centrifugal equator from the JRM33 model fits explains the applied data set better than the dipole centrifugal equator. The quadropole moments alter Io's relative position to the torus, which changes the plasma density around Io by up to $\Delta\rho/\rho = 20\%$.

1. Introduction

Io's interaction with the surrounding plasma is an important feature of Jupiter's inner magnetosphere. On the one hand, it feeds the Io Plasma Torus by atmospheric sputtering (e.g., Bagenal & Dols, 2020; Haff et al., 1981; McGrath & Johnson, 1987; Saur et al., 2004, and references therein), where ion–neutral collisions eject particles from Io's atmosphere that generate a neutral torus in Io's orbit. This neutral torus gets successively ionized, forming the Io Plasma Torus. Furthermore, the plasma locally around Io is perturbed by the collision with Io and its atmosphere. These perturbations travel as Alfvén waves along the magnetic field lines and accelerate particles close to Jupiter's ionosphere (Crary, 1997; Damiano et al., 2019; Janser et al., 2022; Szalay et al., 2018, 2020). The accelerated particles travel along the magnetic field lines, generating aurora at both hemispheres (Bonfond et al., 2015; Hess et al., 2010; Saur et al., 2013; Schlegel & Saur, 2022), called the Io Footprint. The location of these footprints depends on the magnetic field model and density model along the magnetic field line and has been used to constrain the VIP4 magnetic field model (Connerney et al., 1998). With the in situ magnetic field measurements from the Juno spacecraft, a precise magnetic field model for the inner Jovian magnetosphere up to 30th degree is available now in the form of the JRM33 (Connerney et al., 2022). Therefore, the position of the Io Footprint can now be used to constrain the density profile along the magnetic field lines and give insight about the density structure and location of the Io Plasma Torus.

The torus is often considered to lie at the centrifugal equator, the position along the magnetic field line farthest away from the rotational axis (Khurana et al., 2004; Thomas et al., 2004). In the case of a dipolar magnetic field, the centrifugal equator is planar, roughly two thirds on the way from the rotational equator to the magnetic equator. However, higher order moments warp the centrifugal equator "like a potato chip" (Herbert et al., 2008; P. H. Phipps et al., 2020). Other previous observation also show a more complex structure of the torus, not consistent with a dipole centrifugal equator (Bagenal, 1994; P. H. Phipps et al., 2020; Schneider & Trauger, 1995). However, the previous work did not demonstrate with quantitative measures that the torus is located at the multipole centrifugal equator.

The aim of this work is to quantitatively demonstrate that the plasma torus is centered on the multipole centrifugal equator. Therefore, we use the positions of the Io Footprint to constrain a density model of the Io Plasma Torus and its location depending on System III longitude. For that, we map Alfvén waves along the magnetic field lines

and compare the resulting expected location of the footprint to Hubble Space Telescope observations and infer Alfvén wave travel times. We use these travel times as an input for an inversion and analyze the output regarding the hypothesis of a dipole or multipole centrifugal equator.

2. Model and Methodology of the Inversion

2.1. Location of the Io Footprints

When Jupiter's corotating plasma collides with Io and its tenuous atmosphere, it gets perturbed. These perturbations propagate as Alfvén waves along the magnetic field lines that are frozen into the plasma. Close to Jupiter in the acceleration region, these waves cause wave–particle interaction and accelerate particles toward and away from Jupiter. The accelerated particles collide with molecules in Jupiter's upper atmosphere and create auroral emissions. Since the accelerated particles travel along the magnetic field lines and the Alfvén velocity close to Jupiter approaches the speed of light, the exact height of the acceleration region or the emissions does not affect the travel time significantly and we can assume that the emissions are created at the location where the Alfvén waves connect to Jupiter's atmosphere. Therefore, we assume that Io's main footprint is located at the position of Io's main Alfvén wing (MAW) on Jupiter's 1 bar level.

Since the Alfvén waves get reflected at phase velocity gradients, which are most prominent at Jupiter's ionosphere and the Io torus boundary, there is a multitude of secondary footprints. Furthermore, the particles in the acceleration region are also accelerated away from Jupiter, creating footprints on the opposing hemisphere, which can result in leading spots that are upstream from the MAW-footprint. This work only focuses on the location of the MAW-footprints, since the secondary spots are dependent on the reflection pattern and the leading spot is affected by broadening due to electron drifting of about $\Delta\varphi \approx 0.7°$ corresponding to $\Delta l \approx 200$ km broadening of the leading spot on Jupiter's surface for high-energy electrons with energies of $E_e = 1$ MeV (Mauk et al., 1997). This results in a difficult determination of the exact position of the leading spot and its corresponding magnetic field line.

The location of the MAW-footprint can be calculated with the Alfvén characteristic

$$z^{\pm} = \mathbf{v} \pm \mathbf{v}_A, \tag{1}$$

with the plasma velocity $\mathbf{v}$ and the Alfvén phase velocity

$$\mathbf{v}_A = \frac{\mathbf{B}}{\sqrt{\rho\mu_0}}, \tag{2}$$

depending on the magnetic field strength $\mathbf{B}$ and the plasma mass density ρ. Since at high latitudes, the plasma is very dilute, a relativistic correction for the Alfvén velocity has to be implemented:

$$v_A^* = \frac{v_A}{\sqrt{1 + v_A^2/c^2}}. \tag{3}$$

2.1.1. HST Observations

The position of the footprints relative to Io can be described as leading angle $\varphi = \varphi_{Io} - \varphi_F$, which is the longitudinal difference between Io's orbital position φ_{Io} and the Io Footprint φ_F in System III coordinates. The positions here are projected to a height of 900 km above the 1 bar level of Jupiter. The data used here have been published as supplementary material by Bonfond et al. (2017) and are shown in Figure 1. The observations have been mostly conducted between February and June 2007. For the northern footprint, additional data from 2005 to 2006 have been used. The errors ε_φ are mostly due to inaccuracies in the determination of Jupiter's position using the limb fitting method as described in Bonfond et al. (2009). This likely leads to systematic errors in the longitudinal position of the footprints. Furthermore, the observations of the same visit cannot necessarily be regarded as independent from each other. This would mean that the errors of clustered data might be correlated. Close to the limb of Jupiter, the error bars grow larger on account of projection effects.

2.1.2. The Magnetic Field Model

The Alfvén waves travel along the magnetic field lines that in this model are assumed to be fixed in Jupiter's rotating frame. Therefore, the location of the footprints only depends on the magnetic field lines connecting Jupiter's ionosphere to Io's orbit. This leads to all Io Footprints to be confined to one line on the surface of

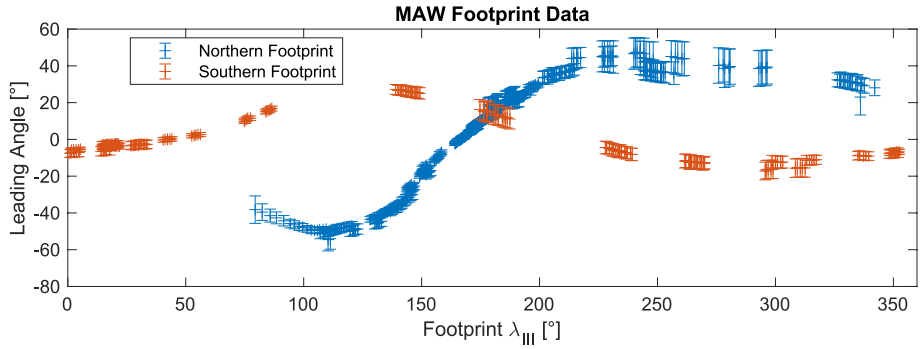

Figure 1. Leading angles of the northern (blue) and southern (red) footprint, calculated from the observations published in Bonfond et al. (2017). Many of the data points are clustered, especially visible for the southern footprint. The lack of observations between 0° and 70° for the northern footprint is because of the high angular velocity of the footprint in this area. Therefore, the footprint remains at this range only for a short time (≈50 min).

each Jovian hemisphere. Though the magnetic field in Io's vicinity can often be regarded as a dipole of strength $M = 4.177$ G and a latitudinal tilt of $\vartheta_D = 10.25°$ in $\varphi_D = 196.38°$ western longitude, the magnetic field closer to Jupiter is more complex. We calculated the footprint trajectories as shown as black lines in Figure 2 using the JRM33 magnetic field model by Connerney et al. (2022). This model has been created using the magnetic field data of the first 33 Juno flybys. We used all available Gauss coefficients g_l^m and h_l^m up to degree $l = 30$ to map Io's orbit to the dynamically flattened (1/15.4) surface of Jupiter along the magnetic field lines to Jupiter's 1 bar level (Connerney et al., 2022).

As can be seen, the footprints are generally drawn toward higher magnetic field strength. Since the magnetic field in the Northern Hemisphere is more complex than in the Southern Hemisphere, the trajectory there spans over a broader range of latitude ($45° < \vartheta_F < 83°$). Furthermore, the separation between the footprint mappings is smaller where the magnetic field is stronger, which implies a slower movement of the Io Footprint over Jupiter's surface as shown in Figure 3. There, the travel time has a lower influence on the leading angle φ than at locations where the spacing is larger. The leading angles φ_B that only result from the magnetic field model are shown in Figure 4, where no travel time of the Alfvén waves is assumed. Here, the change of the leading angles $\dot{\varphi}_B = \dot{\varphi}_{Io} - \dot{\varphi}_F$ only depends on the difference of the angular velocities of the footprints $\dot{\varphi}_F$ (solid lines in Figure 3) and Io $\dot{\varphi}_{Io}$ (yellow dashed line in Figure 3). Qualitatively, the observations (black with error bars) match the behavior of the results of the calculations (solid lines). Since no travel time is included here, the calculations are generally underestimating the leading angles. Where the travel time has low influence, for example, between 150° and 200° for the northern footprint (blue), the observations are fairly well matched already. On the other hand, where travel time

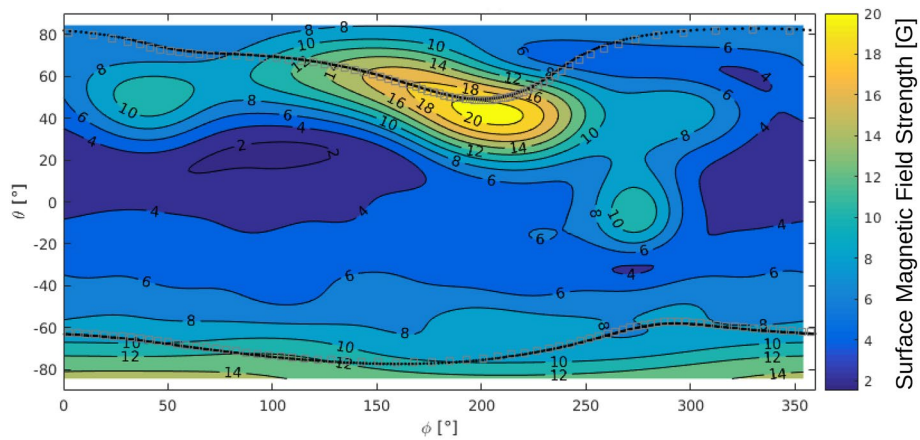

Figure 2. The magnetic field strength on the flattened surface of Jupiter, calculated with the JRM33 model (Connerney et al., 2022). The black dots indicate the trajectory of the Io Footprint in the Northern and Southern Hemisphere in 1° longitudinal separations along Io's orbit. The gray squares are the observational positions of the Io Main Footprints.

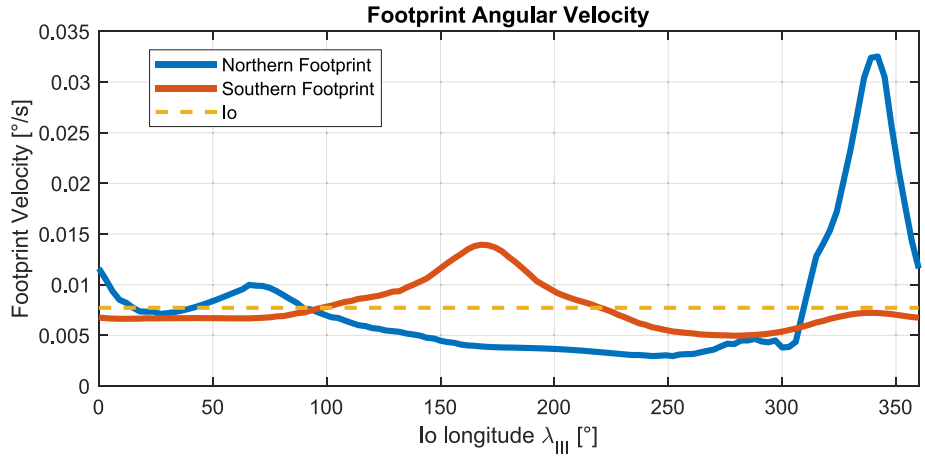

Figure 3. The longitudinal angular velocity of the northern (blue) and southern (red) footprint. The synodical angular velocity of Io is shown as a reference as yellow dashed line at about 0.0077°/s. The northern magnetic field is more structured leading to a more variable angular velocity of the northern footprint.

has a strong influence, for example, close to 0° for the northern footprint, the mapping strongly overestimates the observations.

2.1.3. Influence of the Io Plasma Torus Mass Density

The Io Plasma Torus is generally assumed to be centered on the centrifugal equator of Jupiter's magnetosphere, that is, the position along the magnetic field lines that map toward Io's orbit and is the farthest away from Jupiter's rotation axis. A tilted or an offset tilted dipole results in the torus to be confined on a plane tilted by $\theta_C = 6.83°$ in the direction of $\varphi_D = 196.28°$ western longitude. However, moments of higher degree, especially quadropole, still have an influence of the magnetic field at Io's orbit (P. H. Phipps et al., 2020). The discrepancy between of the latitudinal position of the centrifugal equator using the JRM33 full magnetic field model and only the dipole components can be up to 1.5°, which translates to about $\approx 0.15 R_J$ or $\approx 6 R_{Io}$. The centrifugal equator is a good estimate for the position of the plasma torus as it is derived from the force balance between pressure force and centrifugal force along the magnetic field lines.

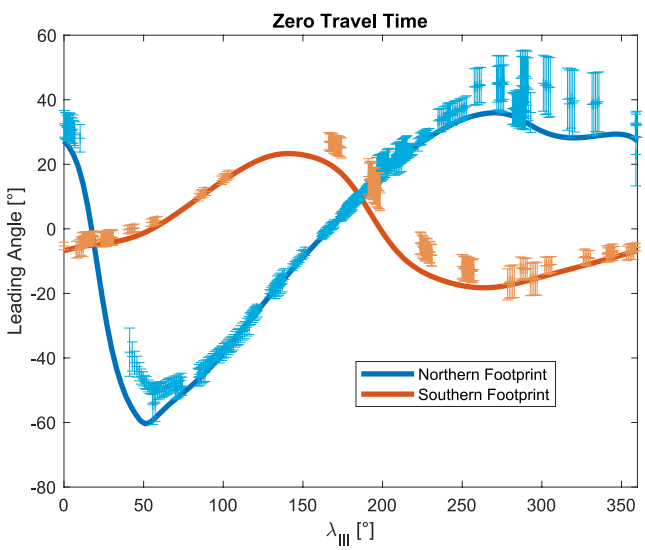

Figure 4. The leading angle without travel travel time assumed for the northern (red) and southern (blue) footprint. The leading angle mostly underestimates the data (black with error bars), since the travel time increases the leading angle. This is especially apparent between 270° and 90° for the northern and 150° and 270° for the southern footprint, where Io should be closer to the southern and northern torus boundary, respectively.

The torus itself is often regarded to be split in three parts (e.g., Bagenal & Dols, 2020; P. H. Phipps et al., 2018, and references therein). The cold torus inside the orbit of Io, the ribbon region, where the plasma density is highest and warm torus starting roughly at the orbit of Io and decreases in density outward. Io itself mostly is located inside the warm torus, but due to a dawn–dusk asymmetry, Io's orbit can cross into the ribbon region (Barbosa & Kivelson, 1983).

The most widely used model for the density distribution ρ is in the form of

$$\rho(s) = \rho_0 \exp\left[-s^2/H^2\right], \tag{4}$$

with a peak density ρ_0 at the centrifugal equator and a Gaussian decrease with distance s to the torus center along the magnetic field line (Bagenal, 1994; Gledhill, 1967; P. H. Phipps et al., 2018, 2021). This coincides with a force balance between centrifugal force and pressure gradient for an isothermal plasma. The scale height H and plasma temperature T are related (Thomas et al., 2004) and can be approximated by

$$H = \sqrt{\frac{2 k_B T}{3 \Omega_J \langle m \rangle}}, \tag{5}$$

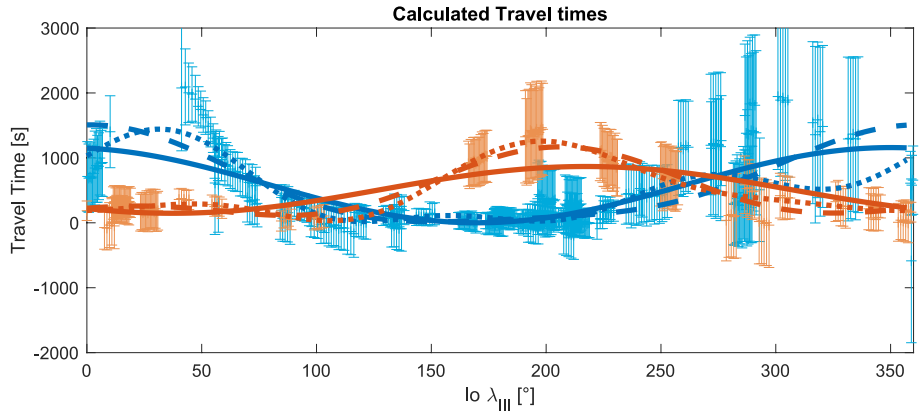

Figure 5. The calculated travel times for the northern (blue) and southern (red) footprints with their corresponding error bar ε_t. The solid line is a first degree fit and the dashed lines is a second degree Fourier fit using Equation 6. The values are computed from the JRM33 (Connerney et al., 2022) mapping and the footprint data published by Bonfond et al. (2017).

with Jupiter's rotational frequency Ω_J and the mean ion mass $\langle m \rangle$. Dougherty et al. (2017) also use pressure anisotropy, ambivalent electric fields, and multiple species to derive a density distribution along the magnetic field line. However, in this work, we will use a simplified density model of the form of Equation 4 in order to reduce the amount of fitting parameters for the inversion.

Hinton et al. (2019) used the JRM09 magnetic field model (Connerney et al., 2018) and the CAN model (Connerney et al., 1981) together with the density model by Dougherty et al. (2017) to calculate travel times from Io's orbit toward Jupiter. The authors fitted the travel times with a third degree Fourier series corresponding to

$$t_{\mathrm{Fit}}(\lambda_{\mathrm{III}}) = \underbrace{A_0 + A_1 \cos(\lambda_{\mathrm{III}} + a_1)}_{1\mathrm{st}} + \underbrace{A_2 \cos(2\lambda_{\mathrm{III}} + a_2)}_{2\mathrm{nd}} + \underbrace{A_3 \cos(3\lambda_{\mathrm{III}} + a_3)}_{3\mathrm{nd}} \tag{6}$$

and found average travel times of 433 and 401 s for the Northern and Southern Hemisphere, respectively. The difference is due to the asymmetry of the magnetic field. In this work, we use the travel times to constrain a density model corresponding to Equation 4 with a peak density at the centrifugal equator. To visualize the data shown in Figure 1 for that purpose more clearly, the leading angles have been converted to travel times t_0 using the synodic angular velocity Ω_{syn} of Io around Jupiter with

$$t_0 = \frac{\varphi_{\mathrm{Io}} - \varphi_{\mathrm{F}}}{\Omega_{\mathrm{syn}}}. \tag{7}$$

Furthermore, the errors are due to inaccuracies in the determination of the footprint positions, but not the position of Io. Therefore, the error in travel time $\varepsilon_t = \varepsilon_\varphi / \dot{\varphi}_{\mathrm{F}}$ has to be weighted corresponding to the current longitudinal velocity of the footprint according to Figure 3. The calculated travel time data are depicted in Figure 5. The data have been fitted using a Fourier fit up to degree three corresponding to Equation 6. The misfits $\chi = \sqrt{1/N \sum (t_0 - t_{\mathrm{Fit}})^2 / \varepsilon_t^2}$ are 0.76, 0.68, and 0.65 for the northern and 0.63, 0.38, and 0.30 for the southern footprint for the fits of degree one, two, and three, respectively. The fitting values are shown in Table 1 together with the values calculated from the model of Dougherty et al. (2017) by Hinton et al. (2019).

Overall the average travel time calculated from the footprint positions is slightly higher and the travel times are more variable compared the values calculated from the model by Dougherty et al. (2017). The higher travel times indicate slower Alfvén velocities and therefore an overall higher plasma content of the torus. The higher variability of the travel times implies a larger influence of Io's relative distance to the torus center, which could be explained by either a more variable torus position or a smaller scale height. Another interesting fact is that the southern travel times are generally shorter and overall less variable due to the more homogeneous magnetic field in the south. Therefore, the southern travel times reflect the plasma density along the field line better than the northern travel times. The variation of travel times can mostly be explained by a relative shift of Io's position with respect to the torus center. Therefore, the strong decrease in misfit from first to second degree Fourier series already shows that a warped centrifugal equator due to quadropole moments fits the data much better than an

Table 1
Fits of the Travel Time Up To Third Degree According to Equation 6, Corresponding to the Curves Shown in Figure 5

Fit/model	A_0 (s)	A_1 (s)	a_1 (°)	A_2 (s)	a_2 (°)	A_3 (s)	a_3 (°)
First degree north	579.4	−579.3	−170.44	0	0	0	0
Second degree north	603.6	−728.2	−178.3	175.0	−12.3	0	0
Third degree north	534.5	−526.6	178.9	246.0	2.8	23.0	−100.5
Hinton et al. north	432.9	289.3	−104.3	21.2	77.0	8.4	46.7
First degree south	507.1	360.7	142.5	0	0	0	0
Second degree south	478.1	456.4	161.8	236.0	−51.0	0	0
Third degree south	479.2	440.1	146.8	266.5	−45.4	11.3	−162.4
Hinton et al. south	400.7	260.7	65.2	19.4	−87.9	10.5	−155.9

Note. As a reference, the third degree fit of the travel times calculated by Hinton et al. (2019), based on the model by Dougherty et al. (2017) are given.

offset dipole centrifugal equator. The fits of the northern footprints are mostly constrained by the observational data between 130° and 200° which have fairly small error bars. However, all fits show an a_1 value of around 180°, which indicates that the torus is tilted in line with the dipole tilt of the JRM33 model of $\varphi_D = 196.38°$. The fairly small decrease in misfit from second to third degree fits (0.03 for the northern and 0.08 for the southern footprints) hints that the position of the torus is mostly constrained by dipole and quadropole moments.

2.2. Cost Function and Inversion Method

The travel time data, converted according to Equation 7, are now fitted using a density model corresponding to Equation 4. The cost function Φ of this inversion scheme can be written as

$$\Phi = \sum_i \left(\frac{t_{0,i} - t_{\rho,i}}{\varepsilon_{t,i}} \right)^2, \tag{8}$$

with the calculated travel times

$$t_\rho(\rho_0, H) = \int_{\mathrm{Io}}^{J} \frac{1}{v_A^*} ds \tag{9}$$

mapped along the magnetic field line. It is important to note that the field line connected to the footprint is used since this is the field line that the Alfvén waves propagate on starting from Io's position. To minimize the cost function, a Monte-Carlo inversion method has been used to sweep the parameter space. For the scale height H values between $H_{\min} = 0.4R_J$ and $H_{\max} = 1.6R_J$ and for the peak number density $n_0 = \rho_0/\langle m \rangle$ values between $n_{\min} = 500\ \mathrm{cm}^{-3}$ and $n_{\max} = 3{,}500\ \mathrm{cm}^{-3}$ have been used. With this approach, the sensitivity of the inversion toward the fitting parameters H and ρ as well as the correlation between them can be analyzed.

3. Inversion Results

In a first step, the travel times are fitted for the peak density located at both, the dipole and the JRM33 multipole centrifugal equator and compared to values in the literature. In a second step, the position of the torus is fitted separately in another inversion to evaluate, whether the dipole or multipole centrifugal equator explains the data better.

3.1. Best Fit Models

For the first inversion, the peak density n_0 is located at the JRM33 dipole and multipole centrifugal equator. The resulting leading angles are shown in Figure 6. For the dipole model, the values for peak density and scale height are $n_0 = 1{,}900\ \mathrm{cm}^{-3}$ and $H = 1.01R_J$, while for the multipole model the values are $n_0 = 2{,}133\ \mathrm{cm}^{-3}$ and $H = 1.07R_J$, respectively. The two models do not differ much in travel times and therefore in leading angle. However, the

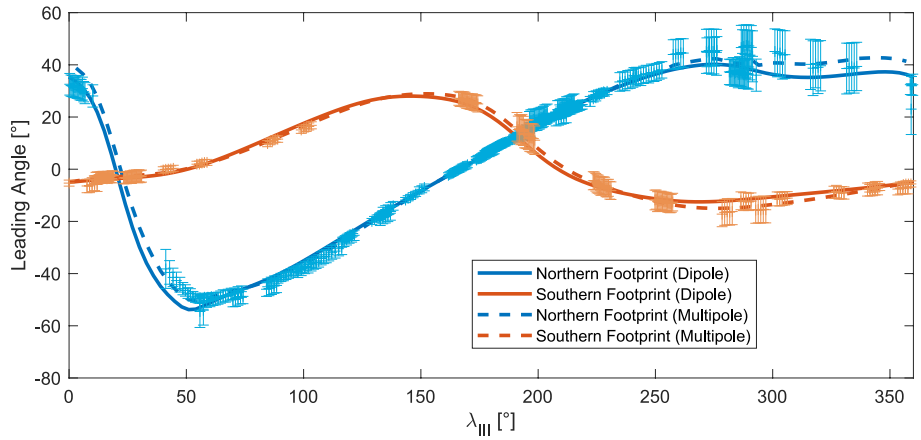

Figure 6. The best fit models for the northern (blue) and southern (red) leading angles for both, the dipole (solid line) and multipole (dashed) centrifugal equator model. The multipole model generally fits the data better.

misfit of $\chi = 0.58$ of the multipole best fit is considerably improved compared to the misfit of $\chi = 0.78$ of the dipole model. This is mostly due to some very low error observations of the southern footprint between 50° and 100° eastern longitude. For the southern footprint, the density model has a more consistent impact on the travel time and leading angle due to the longitudinal more homogeneous magnetic field. In Figure 7, the misfit for the whole Monte-Carlo inversion parameter domain is shown for both models. Since the errors of the observation are considerably large and comparable to the overall travel time (compare Figure 5), a large parameter space can fit the observations with a misfit of $\chi < 1$. This allows us to estimate an uncertainty to the best fit parameters. For the dipole model, we find $\Delta n_0 = 321$ cm^{-3} and $\Delta H = 0.13 R_J$. For the multipole model, the uncertainties are larger due to the overall better fit, and we get $\Delta n_0 = 413$ cm^{-3} and $\Delta H = 0.17 R_J$. We can further compare the best fit models to the values given by P. H. Phipps et al. (2018) for the warm torus and ribbon region and Dougherty et al. (2017) and Bagenal (1994) for the vicinity of Io's orbit, shown as stars in Figure 7. Generally, the values in the literature are higher in both peak density and scale height but are mostly inside the $\chi < 1$ region for the multipole centrifugal

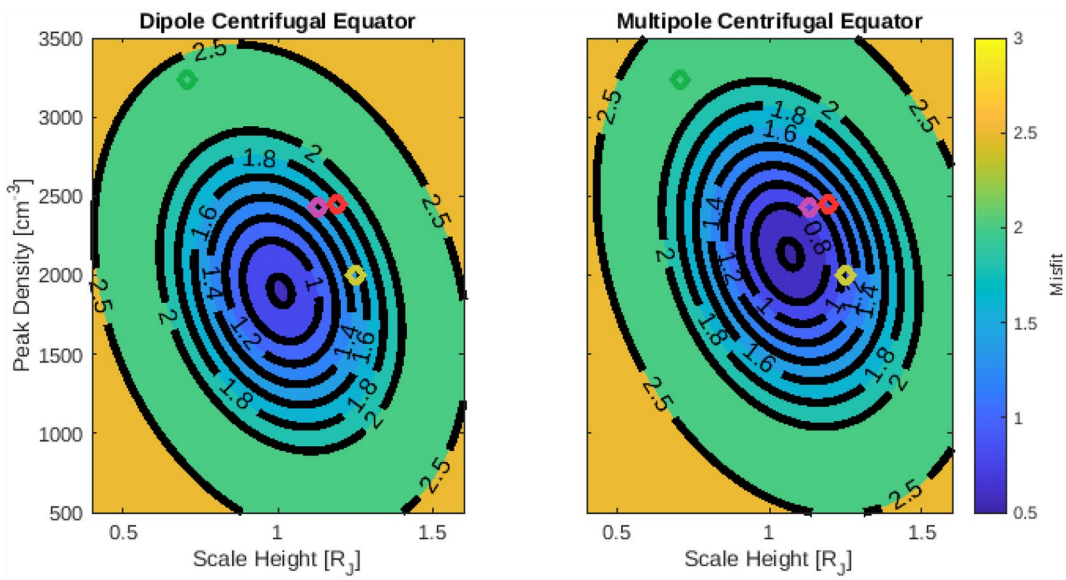

Figure 7. Misfit contour of the Monte-Carlo inversion for the dipole (left) and multipole (right) centrifugal equator model. The peak density and scale height for the warm torus (purple) and ribbon (green) of the model of P. H. Phipps et al. (2018) as well the model by Bagenal (1994) (yellow) and Dougherty et al. (2017) (red) are indicated as diamonds. The scale height of the latter two are calculated with Equation 5.

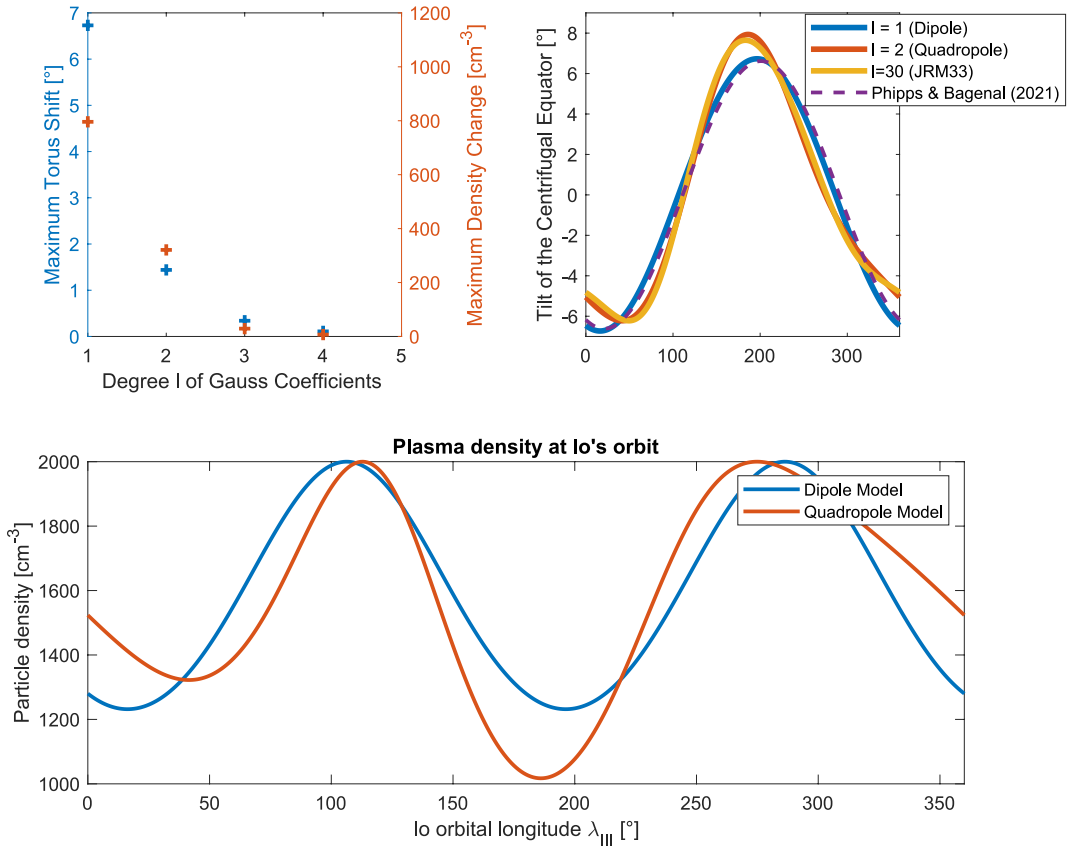

Figure 8. The position of the centrifugal equator has been calculated with different degrees l of the JRM33 model. The position of the centrifugal equator relative to the rotational equator for dipole ($l = 1$), quadropole ($l = 2$), and full JRM33 model ($l = 30$) is shown on the right upper panel and compared to the model by P. Phipps and Bagenal (2021) (Equation 2) at the distance of Io as shown by the purple dashed line. From the variation for different degrees of Io's relative position to the torus center (blue in left panel), the maximum density variation due to the higher degrees in Io's vicinity has been calculated (red in left upper panel) using a scale height density model according to Equation 4. As can be seen, the quadropole moment of the JRM33 model is sufficient to calculate the position of the centrifugal equator at Io's orbit. The lower panel shows the plasma number density at Io's orbit for the dipole and quadropole centrifugal equator model. A peak density of $n_0 = 2{,}000\ \mathrm{cm}^{-3}$ and a scale height of $H = 1R_J$ is used. The maximum difference between the two models is at $\lambda_{III} = 180°$ at about $\Delta\rho \approx 250\ \mathrm{cm}^{-3}$.

equator. The results of the inversion overall show a good agreement with the literature, especially the results of the multipole model inversion.

To quantify the improvement of the multipole centrifugal equator, a Monte-Carlo Test was performed. In this test, each data point has been randomized with Gaussian noise corresponding to their calculated error added to their value. The number of data points that are fitted by one model rather than the other has been counted. This procedure has been repeated $N = 100{,}000$ times. In the end, 91.4% of randomized data points are fitted better by the multipole centrifugal equator and only 8.6% of data points are fitted better by the dipole centrifugal equator model.

3.2. Position of the Io Plasma Torus

We conducted a study to investigate to what degree the JRM33 multipole moments influence the position of the Io Plasma Torus and therefore the density in Io's vicinity. In this study, we first calculated change in the position of the Io Plasma Torus with each additional degree of the Gauss coefficients of the JRM33 model as can be seen in the upper left panel in Figure 8. From that, the variation of Io's relative position to the torus center due to each additional degree up to $l = 5$ has been calculated (blue on upper right panel). We then used a torus density model according to Equation 4 with a peak density of $\rho_0 = 2{,}000\ \mathrm{cm}^{-3}$ and a scale height of $H = 1R_J$ to calculate the

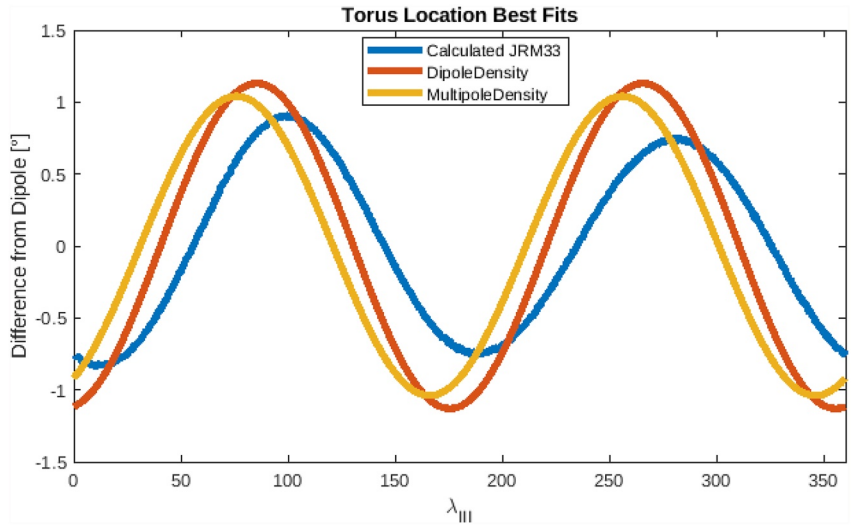

Figure 9. Best fit models for the torus positions for the best fit peak density and scale height of the dipole (red) and multipole (yellow) model inversions. Phase and amplitude of both best fit models are comparable to the location of the JRM33 multipole centrifugal equator, shown in blue. Therefore, the location of Io's footprint clearly indicates a pi-periodicity in the Alfvén wave travel times and therefore in Io's relative position to the torus center. A purely dipole centrifugal equator is not sufficient to explain the data.

maximum density change in Io's vicinity due to each additional degree. As can be seen, the density changes less then $\Delta\rho < 20$ cm^{-3} for higher moments $l > 3$. We therefore conclude that the quadropole moments are sufficient to describe the position of the torus.

To estimate the effect of the shift in position of the plasma torus due to the quadropole moments on the plasma density in Io's vicinity, we calculated the density at Io's orbit for a dipole and quadropole model. The results are shown in the lower panel of Figure 8. The largest discrepancy between the two models is around $\lambda_{III} = 180°$, where the density differs about $\Delta\rho \approx 250$ cm^{-3} or $\Delta\rho/\rho \approx 20\%$.

3.2.1. Inversion of the Plasma Torus Position

To test, whether the multipole centrifugal equator generally fits the data better, the position of the torus is also inverted. Since the data can be fitted by a large parameter space for two parameters already, we refrain from adding more inversion parameters. Instead, we use the values of peak density and scale height from the best fit models in the last section and use the amplitude θ_0 and phase $\Delta\lambda$ of the pi-periodicity of the location of the torus corresponding to the quadropole moments as new inversion parameters. The lateral displacement θ of the torus to the rotational equator can be written as

$$\theta(\lambda_{III}) = \theta_D(\lambda_{III}) + \theta_0 \sin(2\lambda_{III} + \Delta\lambda), \tag{10}$$

where θ_D is the tilt of the dipole centrifugal equator with $\theta_D(196.38°) = -6.83°$. The displacement from dipole centrifugal equator resulting from the inversions is shown in Figure 9. The dipole model ($n_0 = 1{,}900$ cm^{-3}, $H = 1.01R_J$) best fit parameters are $\theta_0 = 1.13°$ and $\Delta\lambda = 81°$ with a misfit of $\chi = 0.61$ compared to the previous misfit with $\theta_0 = 0°$ of $\chi = 0.78$. The multipole model ($n_0 = 2{,}133$ cm^{-3} and $H = 1.07R_J$) best fit parameters are $\theta_0 = 1.04°$ and $\Delta\lambda = 62°$ with a misfit of $\chi = 0.52$. Generally the fit improves, however not significantly for the multipole model, where the position of the torus already seems to be sufficient. The new best fit torus positions are comparable to the JRM33 multipole centrifugal equator position (blue line in Figure 9) in phase and amplitude. This and the significant decrease in misfit for the dipole centrifugal equator model indicate that the torus is indeed located at the centrifugal equator of the JRM33 magnetic field model rather than a simple dipole centrifugal equator.

4. Summary and Conclusion

We used Hubble Space Telescope observations of the Io Main Footprint as data to constrain a density model for the Io Plasma Torus. In this model, we used the JRM33 magnetic field model by Connerney et al. (2022) to map the magnetic field lines connecting the footprints to Io's orbit to calculate leading angle and Alfvén wave travel time. The travel time has then been used as data for a Monte-Carlo inversion to constrain peak density and scale height of the torus. In the first two inversions, the position of the plasma torus is fixed once at the dipole centrifugal equator and once the multipole centrifugal equator of the JRM33 magnetic field model. The results show peak densities of $n_0 = (1{,}900 \pm 321)$ cm^{-3} and $n_0 = (2{,}133 \pm 413)$ cm^{-3} and scale heights of $H = (1.01 \pm 0.13)R_J$ and $H = (1.07 \pm 0.17)R_J$ for the dipole and multipole model, respectively. These values are in agreement, albeit generally lower than those of other models in the literature. Both models fit the data well. However, the misfit $\chi = 0.58$ of the multipole model is significantly lower than the misfit $\chi = 0.78$ of the dipole model. This agrees with a Monte-Carlo test, where 91.4% of the data points are better fitted by the multipole model.

In a second set of inversions, the position of the plasma torus is fitted. The amplitude and phase shift of the lateral displacement are used as inversion parameters while scale height and peak density are kept fixed. The results show an agreement with the predicted JRM33 multipole centrifugal equator location of the Io Plasma Torus.

It could be shown that this method is suitable to constrain peak density and scale height of the Io Plasma Torus and yields results comparable to literature values. We demonstrate quantitatively that the torus is warped along the multipole centrifugal equator and the data cannot sufficiently be explained by a simple dipole centrifugal equator. The latitudinal shift from a dipolar compared to a multipole centrifugal equator can differ by up to 1.5° which translates to a change of Io's relative position to the torus center to up to $0.15R_J \approx 6R_{\mathrm{Io}}$. In addition of the synodic period variation of $\Delta\rho \approx 800$ cm^{-3}, Io is exposed to a half synodic density variation of $\Delta\rho \approx 250$ cm^{-3}, which corresponds to a maximum in relative change of $\Delta\rho/\rho = 20\%$. This needs to be included in high-precision models of the Io plasma interaction to, for example, model the atmospheric sputtering processes or the evolution of the Io Footprint brightness. The latter might be less faint near the minimum around 180° compared to minimum around 330° (Wannawichian et al., 2010).

The method presented here uses the integrated travel times of the Alfvén waves and is therefore able to constrain the mass density along the Io flux tube. However, the currently available data are not sufficient to distinguish between different species and scale heights of different populations. Furthermore, the nonuniqueness of the inversion method hinders an interpretation regarding a more complex density model. Nevertheless, with additional observations and more accurate positions of the Io main and reflected footprint, this method could provide further insights into the density structure along the Io flux tube. Additional data could be used to constrain longitudinal and time variability and the density model could be adapted to incorporate the effect of different species and scale heights.

Data Availability Statement

The processed travel times according to Equation 7 and Figure 5, the used magnetic field mapping using the JRM33 model, and the inversion results as shown in Figure 7 are available and published in Schlegel and Saur (2023).

Acknowledgments
This project has received funding from the European Research Council under the European Union's Horizon 2020 research and innovation program (Grant 884711). This research was supported by the International Space Science Institute (ISSI) in Bern, through ISSI International Team project 515. Open Access funding enabled and organized by Projekt DEAL.

References

Bagenal, F. (1994). Empirical model of the Io Plasma Torus: Voyager measurements. *Journal of Geophysical Research*, *99*(A6), 11043–11062. https://doi.org/10.1029/93JA02908

Bagenal, F., & Dols, V. (2020). The space environment of Io and Europa. *Journal of Geophysical Research: Space Physics*, *125*, e2019JA027485. https://doi.org/10.1029/2019JA027485

Barbosa, D., & Kivelson, M. (1983). Dawn–dusk electric field asymmetry of the Io Plasma Torus. *Geophysical Research Letters*, *10*(3), 210–213. https://doi.org/10.1029/GL010i003p00210

Bonfond, B., Grodent, D., Gérard, J.-C., Radioti, A., Dols, V., Delamere, P., & Clarke, J. (2009). The Io UV footprint: Location, inter-spot distances and tail vertical extent. *Journal of Geophysical Research*, *114*, A07224. https://doi.org/10.1029/2009JA014312

Bonfond, B., Gustin, J., Gérard, J.-C., Grodent, D., Radioti, A., Palmaerts, B., et al. (2015). The far-ultraviolet main auroral emission at Jupiter—Part 1: Dawn–dusk brightness asymmetries. *Annales Geophysicae*, *33*(10), 1203–1209. https://doi.org/10.5194/angeo-33-1203-2015

Bonfond, B., Saur, J., Grodent, D., Badman, S., Bisikalo, D., Shematovich, V., et al. (2017). The tails of the satellite auroral footprints at Jupiter. *Journal of Geophysical Research: Space Physics*, *122*, 7985–7996. https://doi.org/10.1002/2017JA024370

Connerney, J. E. P., Acuña, M. H., & Ness, N. F. (1981). Modeling the Jovian current sheet and inner magnetosphere. *Journal of Geophysical Research*, *86*(A10), 8370–8384. https://doi.org/10.1029/JA086iA10p08370

Connerney, J. E. P., Acuña, M. H., Ness, N. F., & Satoh, T. (1998). New models of Jupiter's magnetic field constrained by the Io flux tube footprint. *Journal of Geophysical Research*, *103*(A6), 11929–11939. https://doi.org/10.1029/97JA03726

Connerney, J. E. P., Kotsiaros, S., Oliversen, R. J., Espley, J. R., Joergensen, J. L., Joergensen, P. S., et al. (2018). A new model of Jupiter's magnetic field from Juno's first nine orbits. *Geophysical Research Letters*, *45*, 2590–2596. https://doi.org/10.1002/2018GL077312

Connerney, J. E. P., Timmins, S., Oliversen, R. J., Espley, J. R., Joergensen, J. L., Kotsiaros, S., et al. (2022). A new model of Jupiter's magnetic field at the completion of Juno's prime mission. *Journal of Geophysical Research: Planets*, *127*, e2021JE007055. https://doi.org/10.1029/2021JE007055

Crary, F. (1997). On the generation of an electron beam by Io. *Journal of Geophysical Research*, *102*(A1), 37–49. https://doi.org/10.1029/96JA02409

Damiano, P., Delamere, P., Stauffer, B., Ng, C.-S., & Johnson, J. (2019). Kinetic simulations of electron acceleration by dispersive scale Alfvén waves in Jupiter's magnetosphere. *Geophysical Research Letters*, *46*, 3043–3051. https://doi.org/10.1029/2018GL081219

Dougherty, L., Bodisch, K., & Bagenal, F. (2017). Survey of voyager plasma science ions at Jupiter: 2. Heavy ions. *Journal of Geophysical Research: Space Physics*, *122*, 8257–8276. https://doi.org/10.1002/2017JA024053

Gledhill, J. (1967). Magnetosphere of Jupiter. *Nature*, *214*(5084), 155–156. https://doi.org/10.1038/214155a0

Haff, P., Watson, C., & Yung, Y. L. (1981). Sputter ejection of matter from Io. *Journal of Geophysical Research*, *86*(A8), 6933–6938. https://doi.org/10.1029/JA086iA08p06933

Herbert, F., Schneider, N. M., & Dessler, A. (2008). New description of Io's cold plasma torus. *Journal of Geophysical Research*, *113*, A01208. https://doi.org/10.1029/2007JA012555

Hess, S. L., Delamere, P., Dols, V., Bonfond, B., & Swift, D. (2010). Power transmission and particle acceleration along the Io flux tube. *Journal of Geophysical Research*, *115*, A06205. https://doi.org/10.1029/2009JA014928

Hinton, P., Bagenal, F., & Bonfond, B. (2019). Alfvén wave propagation in the Io Plasma Torus. *Geophysical Research Letters*, *46*, 1242–1249. https://doi.org/10.1029/2018GL081472

Janser, S., Saur, J., Clark, G., Sulaiman, A., & Szalay, J. (2022). Properties of turbulent Alfvénic fluctuations and wave–particle interaction associated with Io's Footprint tail. *Journal of Geophysical Research: Space Physics*, *127*, e2022JA030675. https://doi.org/10.1029/2022JA030675

Khurana, K. K., Kivelson, M. G., Vasyliunas, V. M., Krupp, N., Woch, J., Lagg, A., et al. (2004). The configuration of Jupiter's magnetosphere. In *Jupiter: The planet, satellites and magnetosphere* (Vol. 1, pp. 593–616).

Mauk, B., Williams, D., & McEntire, R. (1997). Energy–time dispersed charged particle signatures of dynamic injections in Jupiter's inner magnetosphere. *Geophysical Research Letters*, *24*(23), 2949–2952. https://doi.org/10.1029/97GL03026

McGrath, M., & Johnson, R. (1987). Magnetospheric plasma sputtering of Io's atmosphere. *Icarus*, *69*(3), 519–531. https://doi.org/10.1016/0019-1035(87)90021-2

Phipps, P., & Bagenal, F. (2021). Centrifugal equator in Jupiter's plasma sheet. *Journal of Geophysical Research: Space Physics*, *126*, e2020JA028713. https://doi.org/10.1029/2020JA028713

Phipps, P. H., Withers, P., Buccino, D. R., & Yang, Y.-M. (2018). Distribution of plasma in the Io Plasma Torus as seen by radio occultation during Juno Perijove 1. *Journal of Geophysical Research: Space Physics*, *123*, 6207–6222. https://doi.org/10.1029/2017JA025113

Phipps, P. H., Withers, P., Buccino, D. R., Yang, Y.-M., & Parisi, M. (2021). Two years of observations of the Io Plasma Torus by Juno radio occultations: Results from Perijoves 1 to 15. *Journal of Geophysical Research: Space Physics*, *126*, e2020JA028710. https://doi.org/10.1029/2020JA028710

Phipps, P. H., Withers, P., Vogt, M. F., Buccino, D. R., Yang, Y.-M., Parisi, M., et al. (2020). Where is the Io Plasma Torus? A comparison of observations by Juno radio occultations to predictions from Jovian magnetic field models. *Journal of Geophysical Research: Space Physics*, *125*, e2019JA027633. https://doi.org/10.1029/2019JA027633

Saur, J., Grambusch, T., Duling, S., Neubauer, F., & Simon, S. (2013). Magnetic energy fluxes in sub-Alfvénic planet star and moon planet interactions. *Astronomy & Astrophysics*, *552*, A119. https://doi.org/10.1051/0004-6361/201118179

Saur, J., Neubauer, F. M., Connerney, J., Zarka, P., & Kivelson, M. G. (2004). Plasma interaction of Io with its plasma torus. In *Jupiter: The planet, satellites and magnetosphere* (Vol. 1, pp. 537–560).

Schlegel, S., & Saur, J. (2022). Alternating emission features in Io's footprint tail: Magnetohydrodynamical simulations of possible causes. *Journal of Geophysical Research: Space Physics*, *127*, e2021JA030243. https://doi.org/10.1029/2021JA030243

Schlegel, S., & Saur, J. (2023). *Processed data and inversion results for constraining the Io Plasma Torus*. Zenodo. https://doi.org/10.5281/zenodo.8214702

Schneider, N. M., & Trauger, J. T. (1995). The structure of the Io torus. *The Astrophysical Journal*, *450*, 450. https://doi.org/10.1086/176155

Szalay, J., Allegrini, F., Bagenal, F., Bolton, S., Bonfond, B., Clark, G., et al. (2020). A new framework to explain changes in Io's footprint tail electron fluxes. *Geophysical Research Letters*, *47*, e2020GL089267. https://doi.org/10.1029/2020GL089267

Szalay, J., Bonfond, B., Allegrini, F., Bagenal, F., Bolton, S., Clark, G., et al. (2018). In situ observations connected to the Io Footprint tail aurora. *Journal of Geophysical Research: Planets*, *123*, 3061–3077. https://doi.org/10.1029/2018JE005752

Thomas, N., Bagenal, F., Hill, T., & Wilson, J. (2004). The Io neutral clouds and plasma torus. In *Jupiter. The planet, satellites and magnetosphere* (Vol. 1, pp. 561–591).

Wannawichian, S., Clarke, J., & Nichols, J. (2010). Ten years of Hubble Space Telescope observations of the variation of the Jovian satellites' auroral footprint brightness. *Journal of Geophysical Research*, *115*, A02206. https://doi.org/10.1029/2009JA014456